Available online at https://link.springer.com/journal/42241
http://www.jhydrodynamics.com
Journal of Hydrodynamics, 2026
https://doi.org/10.1007/s42241-026-0040-y

Numerical study of wave breaking under wind forcing

Yu-ming Shao, Jian-hua Wang, De-cheng Wan*

Computational Marine Hydrodynamics Lab (CMHL), School of Ocean and Civil Engineering, Shanghai Jiao Tong University, Shanghai 200240, China

(Received January 19, 2026, Revised February 12, 2026, Accepted February 13, 2026, Published online June 2, 2026)

Abstract: Wave breaking in marine environments frequently occurs under the influence of wind forcing, encompassing intricate processes of energy transfer and interfacial dynamics. This study numerically investigates wave breaking under a range of wind intensities, at high wave steepness conditions. Distinct from traditional studies focusing on wind-driven wave growth, the present work concentrates on energy evolution, spray droplet motion, and bubble dynamics. The results indicate that strong wind forcing significantly enhances the turbulent kinetic energy (TKE) and energy dissipation rate within the water. Wind-driven droplets generated at the jet tip exhibit extended lifetimes and are transported in the wind direction due to complex interactions between initial momentum and turbulence. While the overall bubble count and size distribution remain nearly unaffected, increased wind intensity leads to a shallower vertical distribution of the bubble cloud centroid. These findings provide new insights into wind-induced wave breaking, with implications for understanding marine spray generation and air-sea interaction processes.

Key words: Wind-wave interactions, wave breaking, spume droplets, bubble dynamics

0. Introduction

In nature, the calm sea surface is disturbed by wind, generating the waves as wind energy is converted into wave energy. As wind speed increases, the waves become steeper and eventually break, producing a large number of aerosols and white foams. This process involves complex interfacial dynamics and turbulent mechanisms. Moreover, it generates a large number of splashing droplets and entrained bubbles, which not only influence air-sea exchange and climate systems, but also have important implications for the marine and naval engineering fields. Understanding this process can enhance insight into the impact of wave breaking on ocean structures[1].

Wave breaking under no-wind conditions has been extensively studied over the past several decades through both theoretical analysis and experimental investigations[2-3]. In recent years, advances in computational hardware and numerical algorithms have made high-fidelity numerical simulation an increasingly effective approach. Wang et al.[4] conducted large-scale simulations of 3-D wave breaking using uniform grids, reaching a total grid count of 1.2×10^{10}. Their results captured detailed features of droplet splashing and air entrainment during wave breaking. To reduce computational cost, adaptive mesh refinement (AMR) techniques have been developed, which dynamically increase resolution in regions with strong variations of key physical quantities. Deike et al.[5] employed AMR in conjunction with direct numerical simulation (DNS) to investigate wave breaking mechanisms, categorizing them into parasitic capillary breaking, spilling breaking, and plunging breaking. Further studies[6-7] have also focused on small-scale features such as bubble rising and droplet distributions following wave breaking.

When wind effects are considered, research has mainly focused on two areas: wind-driven wave growth and wind-driven wave breaking[8]. The former investigates the deformation of the free surface under wind forcing. It is generally accepted that wave growth proceeds through a linear stage, driven by three-dimensional turbulence fluctuations, followed by an exponential stage, dominated by the interaction between the mean airflow and the wave surface[9-11]. Wind-induced wave breaking refers to the process in

Project supported by the National Natural Science Foundation of China (Grant Nos. 52131102, 52471335).
Biography: Yu-ming Shao (1998-), Male, Ph. D.,
E-mail: yuming_shao@sjtu.edu.cn
Corresponding author: De-cheng Wan,
E-mail: dcwan@sjtu.edu.cn

which wave steepness increases continuously under wind forcing until the wave breaks. Yang et al.[12] performed three-dimensional DNS to simulate wind-driven wave breaking at various wind speeds, analyzing the transport of turbulent kinetic energy and momentum in the flow field. Cai et al.[13] used a two-dimensional adaptive Cartesian grid solver to carry out parametric studies, examining the effects of wind speed, surface tension, and initial wave steepness on wave breaking. However, most current studies focus on cases with low wave steepness, where the intensity of wave breaking remains moderate. The present study aims to investigate the influence of wind forcing on wave breaking under conditions of high wave steepness, with particular attention to the dynamics of droplet splashing and bubble motion following breaking.

This paper is based on an adaptive Cartesian grid solver framework and explores wave breaking phenomena under various wind speeds. The numerical method is briefly introduced, including the governing equations and free-surface capturing methods. The model setup, mesh generation, and turbulence precursor preparation stage are then described. Finally, the evolution of energy in both air and water, along with the dynamics of splashing droplets and bubble motion under wind forcing, are analyzed and discussed.

1. Numerical method

1.1 *Governing equations*

This study employs the open-source adaptive Cartesian grid solver, Basilisk Flow Solver[14-15]. For incompressible fluids, the governing equations can be expressed as follows:

$$\rho\left[\frac{\partial \boldsymbol{U}}{\partial t}+(\boldsymbol{U}\cdot\nabla)\boldsymbol{U}\right]=-\nabla p+\nabla\cdot(2\mu\boldsymbol{D})+\rho\boldsymbol{g}+\boldsymbol{F}_\sigma \quad (1)$$

$$\nabla\cdot\boldsymbol{U}=0 \quad (2)$$

where $\boldsymbol{U}$ is the fluid velocity, t is the time, p is the pressure, ρ is the density, μ is the fluid dynamic viscosity, $\boldsymbol{D}$ represents the deformation tensor, $\boldsymbol{g}$ is the vector of gravitational acceleration, and $\boldsymbol{F}_\sigma$ is the surface tension term.

1.2 *Free surface capturing*

The coupled level set and volume of fluid (CLSVOF) method is adopted in this study to capture the free surface. This approach ensures mass conservation while providing an accurate geometric representation of the interface. The advection equation is given as follows:

$$\partial_t f+\nabla\cdot(f\boldsymbol{U})=0 \quad (3)$$

$$\partial_t \phi+\nabla\cdot(\phi\boldsymbol{U})=0 \quad (4)$$

where f represents the volume fraction obtained using the VOF-PLIC method, while ϕ denotes the signed distance function used in the level set method.

The surface tension term is modeled using an improved continuum surface force model with balanced forces. To address the issue of inconsistent interface curvature at low resolutions, the method is coupled with the height function curvature technique.

$$\boldsymbol{F}_\sigma=\sigma\kappa(f)\delta_s\boldsymbol{n} \quad (5)$$

where σ is the surface tension coefficient, δ_s is the Dirac delta function localized at the interface, indicating that the surface tension force is applied only at the interface, κ and $\boldsymbol{n}$ denote the interface curvature and the unit normal vector, respectively.

2. Numerical setup

2.1 *Model setup*

As shown in Fig. 1, the computational domain is a square with a side length of $L_0=2\lambda$, where $\lambda=1\,\mathrm{m}$ is the wave length, and two wave crests are distributed along the x- direction. The domain extends from $-0.5\le x/\lambda\le 1.5$ and $0\le y/\lambda\le 2$. The water depth is set to $H_w=0.5\lambda$, and the air height is $H_a=1.5\lambda$. No-slip boundary conditions are imposed on the top and bottom walls, while periodic boundary conditions are applied in the horizontal (left and right) directions.

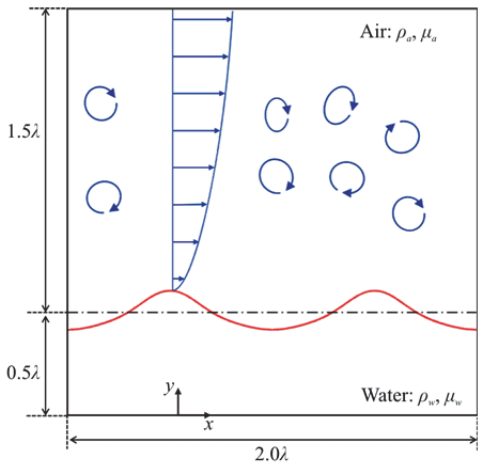

Fig. 1 Schematic diagram of simulation setup

The wave field is initialized using three-order stokes wave to prescribe both the free surface elevation and the velocity distribution:

$$\eta(x)=\frac{1}{2\pi}\left[\varepsilon\cos(2\pi x)+\frac{1}{2}\varepsilon^2\cos(4\pi x)\right.$$

$$+\frac{3}{8}\varepsilon^{3}\cos(6\pi x)\Bigg] \tag{6}$$

$$u_x = a\sqrt{gk(1+\varepsilon^2)}\,\exp(ky)\cos(kx) \tag{7}$$

$$u_y = a\sqrt{gk(1+\varepsilon^2)}\,\exp(kx)\cos(ky) \tag{8}$$

where ε denotes the wave steepness, which is set to 0.6 in this study, a is the wave amplitude, and g is the scalar of gravitational acceleration. The wave-number is given by $k = 2\pi/\lambda$.

The dynamic viscosity ratio between air μ_a and water μ_w is set to $\mu_a/\mu_w = 1.783\times10^{-5}/1.138\times10^{-3}$, and the density ratio between air ρ_a and water ρ_w is $\rho_a/\rho_w = 1/998$. The wave Reynolds number is defined as $Re_w = \rho_w c\lambda/\mu_w = 40\,000$, $c = \sqrt{g/k + \sigma k/\rho_w}$ is wave speed and the Bond number is set to $Bo = (\rho_w - \rho_a)g/\sigma k^2 = 2\,000$. Time is non-dimensionalized using $t^* = t'/T$, where t' computing time, T is the wave period. To facilitate the analysis of energy evolution, turbulent kinetic energy E_k, potential energy E_p, and total energy E_t are defined:

$$E_k = \frac{1}{2}\int \rho u^2 \mathrm{d}x\mathrm{d}y \tag{9}$$

$$E_p = \int \rho g y \mathrm{d}x\mathrm{d}y \tag{10}$$

$$E_t = E_k + E_p \tag{11}$$

2.2 *Precursor preparation stage*

To investigate wave breaking under wind forcing, a precursor simulation is performed to generate a realistic wind field[16-18]. In this approach, the water region is treated as a no-slip boundary using the immersed boundary method, and only the air domain is simulated. Turbulence flow is driven by imposing a constant pressure gradient. It is worth noting that this pressure drive is only added at this precursor preparation stage. The nominal friction velocity u_* is used to characterize the wall stress τ_0:

$$\tau_0 = \rho_a u_*^2 = H_a \frac{\partial p}{\partial x} \tag{12}$$

An AMR strategy is employed, with grid resolution defined as $\Delta = L_0/2^l$, where l is the refinement level. As shown in Fig. 2, a maximum refinement level of $l = 11$ is used, which is sufficient to capture both free-surface breaking and wind field variations in the air phase[17]. The AMR refinement criteria are set as $f_{err} = 1\times10^{-18}$, $u_{a,err} = 0.3u_*$ and $u_{w,err} = 0.001c$.

In this study, simulations were conducted for cases with $u_*/c = 0, 0.3, 0.6, 0.9, -0.9$. Figure 3(a) presents the instantaneous velocity field for the case $u_*/c = 0.9$. The turbulent fluctuation field can be observed on the air side above the wave surface, particularly near the wave crests. Figure 3(b) shows the evolution of air-side turbulent kinetic energy under different conditions. It can be seen that, due to the imposed pressure forcing, the turbulent kinetic energy in the air increases continuously over time. Moreover, higher values of u_*/c lead to a more rapid growth in turbulence intensity.

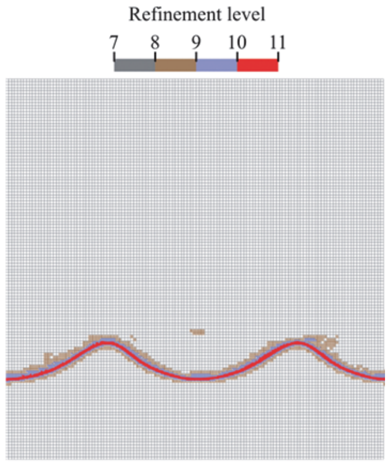

Fig. 2 Schematic diagram of grid adaptive refinement

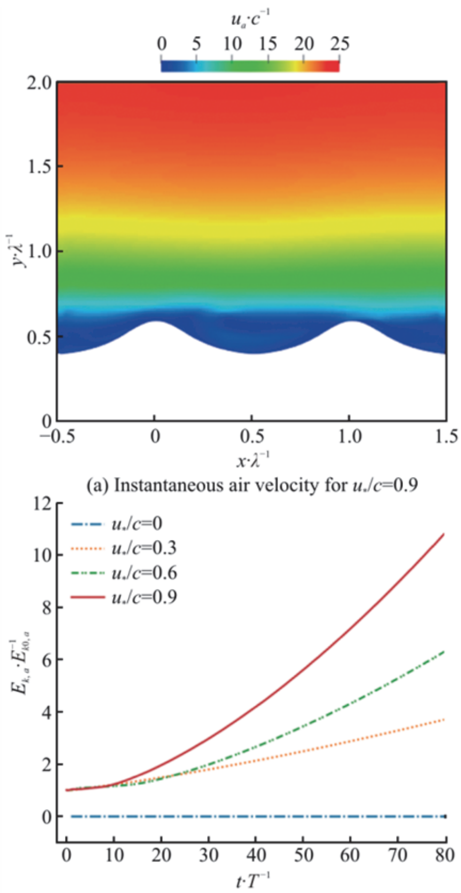

(a) Instantaneous air velocity for u_*/c=0.9

(b) Turbulent kinetic energy (TKE) of the air

Fig. 3 The flow field results of the precursor preparation stage

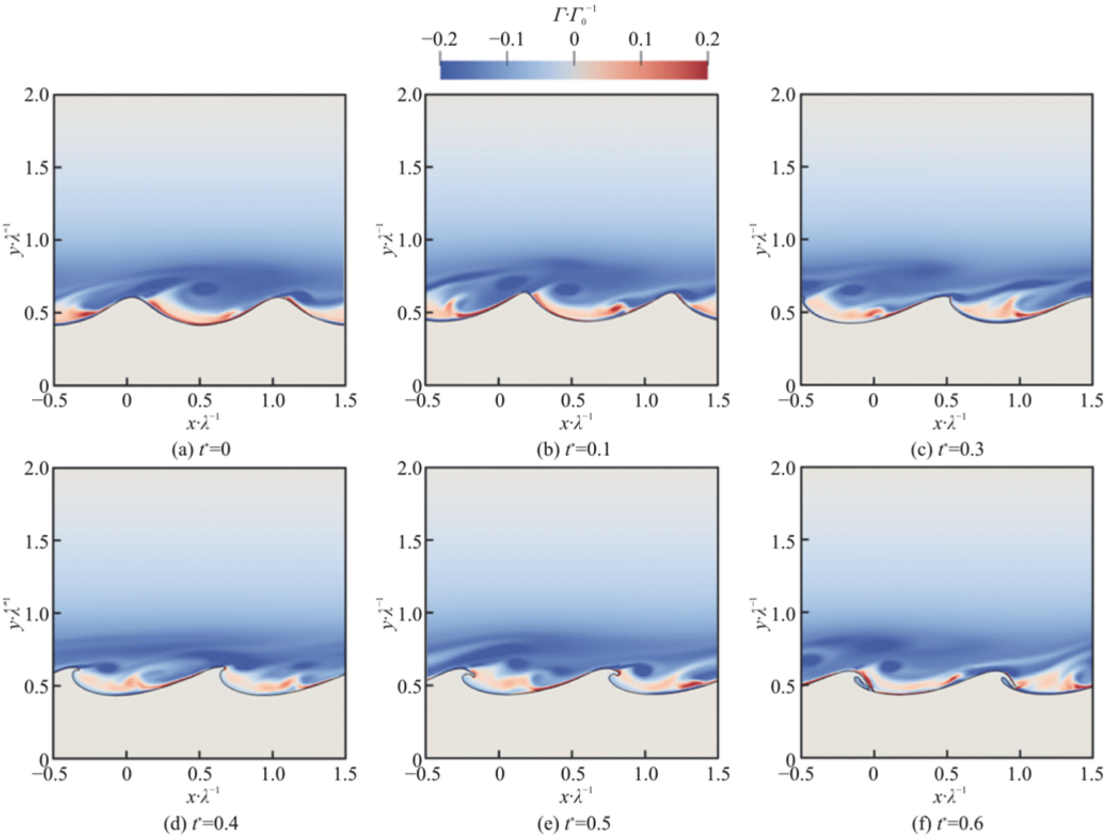

Fig. 4 The evolution of the vortex field in the early stage of wave breaking. The color is vorticity $\Gamma = \partial u / \partial x - \partial u / \partial y$ normalized by the initial velocity profile slope $\Gamma_0 = \rho_a u_*^2 / \mu_a$ [19]

3. Results and discussions

Figure 4 shows the vorticity field during the early stage of wave breaking. As the wave propagates forward, the wind speed exceeds the wave phase speed, resulting in the shedding of pronounced negative vortices near the wave crests. Additionally, the vortices shed from the front and rear interact due to the wave-induced motion. Positive vortices are mainly concentrated in the trough regions.

Figure 5 presents the vorticity field during the wave breaking process. Compared with the initial stage, the vorticity intensity increases significantly, indicating that part of the wave energy is transferred into the air and eventually dissipated. A large number of splashing droplets can be observed. Due to the velocity difference between the droplets and the surrounding air, alternating positive and negative vortices are shed from the trailing edges of the droplets, resembling the vortex street observed in cylinder wake flows. Furthermore, the dominant negative vortex structures in the air grow in volume, entraining droplets and inducing rotational motion.

During the wave breaking process, turbulent kinetic energy in the air is extracted, as shown in Fig. 6. For the case $u_* / c = 0$, the energy in the air is solely supplied by the underlying water, resulting in an initial increase that peaks at approximately $t^* = 1.3$. Subsequently, as wave breaking weakens, the air turbulence gradually diminishes, completing the process of energy transfer and dissipation from the water phase. For the case with $u_* / c = 0.3$, a similar trend is observed, with the air-side turbulent kinetic energy initially increasing and then decreasing. In contrast, for other wind forcing conditions, the turbulent kinetic energy in the air decreases continuously. Particularly during the interval $1 < t^* < 2.8$, which corresponds to the active wave breaking stage, a more rapid dissipation of energy is observed. This effect becomes more pronounced with increasing wind speed, indicating that stronger wind enhances energy dissipation through wave breaking.

Furthermore, the evolution of energy in the water phase is analyzed, as shown in Fig. 7. Figure 7(a) illustrates the temporal variation of TKE in the water. For the cases $u_* / c = 0, 0.3, 0.6$, where wind forcing is relatively weak, the influence on wave breaking is minimal, and the water-side turbulence shows a slight increase followed by a gradual decrease. In the case $u_* / c = 0.9$, the TKE initially increases, exhibiting

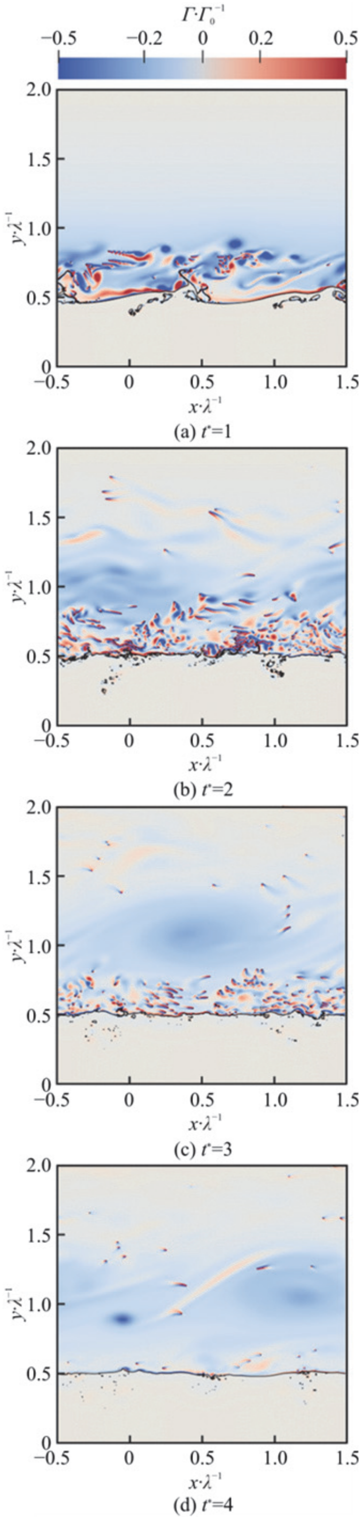

Fig. 5 The evolution of the vortex field during the wave process

three distinct peaks before eventually decreasing. This behavior is consistent with the findings reported in the paper[17], indicating that under strong wind forcing, significant wind energy is injected into the water during wave breaking. For the case $u_*/c=-0.9$, where the wind opposes the wave propagation direction, a slight decrease in TKE is observed during

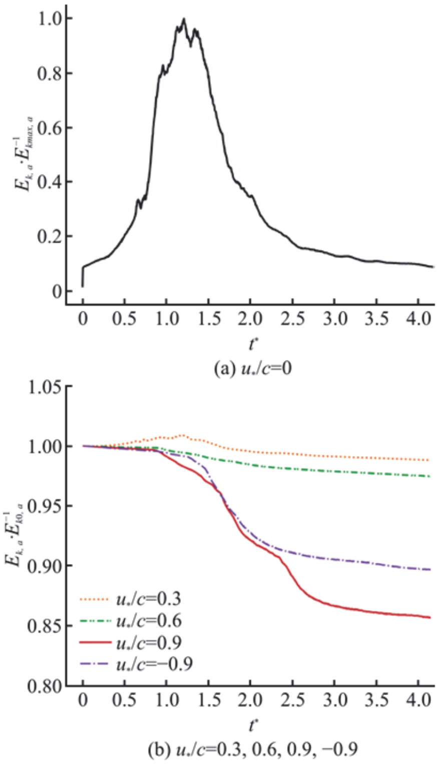

Fig. 6 The time-history curve of TKE of air

the initial stage compared to the no-wind case. However, once wave breaking occurs, the presence of wind rapidly increases the TKE to a peak, followed by a decay. Figure 7(b) shows the temporal evolution of gravitational potential energy. In all cases, the potential energy exhibits an overall decreasing trend. However, under wind-forced conditions, part of the water is lifted into the air as droplets due to wind action, resulting in more fluctuations in the potential energy curve and a slower rate of decline. As shown in Fig. 7(c), the total energy evolution generally follows a trend similar to that of TKE. For $u_*/c=0, 0.3, 0.6$, the total energy decreases continuously. In contrast, for the cases $u_*/c=0.9, -0.9$, an initial increase is observed, followed by a decrease.

Figure 8 shows the energy dissipation rates of the water phase under different wind conditions. For the cases with $u_*/c=0.3, 0.6$, the dissipation rates are similar to that observed in the no-wind case. In contrast, for $u_*/c=0.9, -0.9$, the presence of wind forcing leads to a noticeable increase in the total energy, accompanied by a significantly enhanced dissipation rate. The dissipation profiles under these conditions exhibit multiple pulsating peaks, reflecting the strong and unsteady nature of energy transfer during wave breaking.

Figure 9 presents the instantaneous distribution of droplets during the wave breaking process. At $t^*=0.88, 0.97$, droplets are observed to detach from

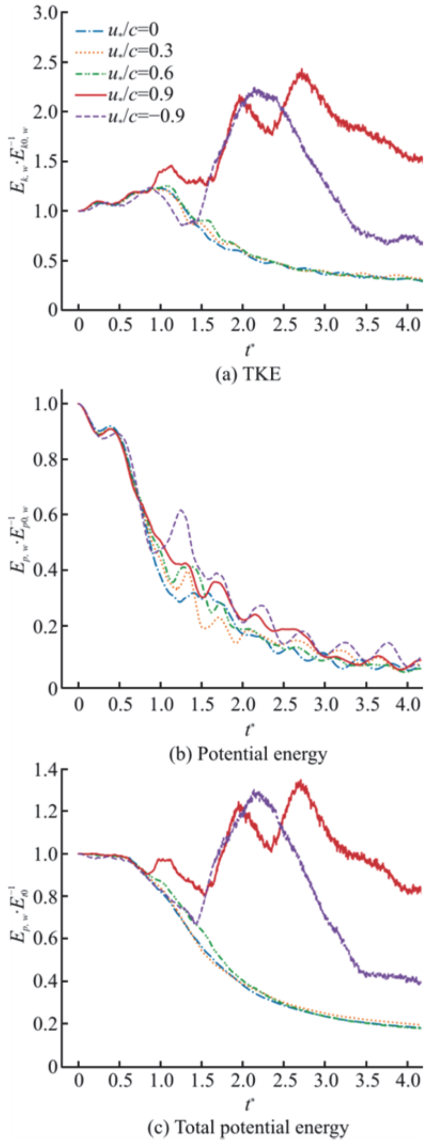

Fig. 7 The time-history curve of water body energy evolution

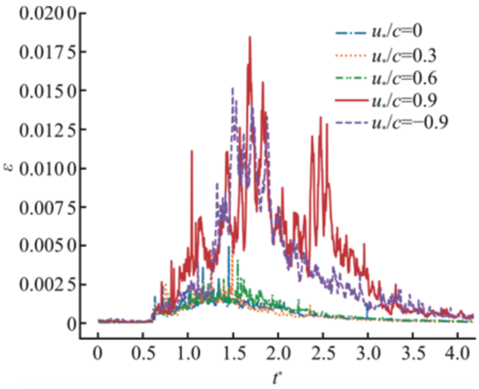

Fig. 8 The energy dissipation rate of water body

the jet tip generated by the breaking wave, with their trajectories aligned with the direction of wave propagation. At $t^* = 1.14, 2.00$, the influence of wind on droplet motion becomes evident. The droplets are distributed at higher altitudes in the air, and due to the irregularity of the free surface breakup, a wider range of velocity directions is observed. At $t^* = 3, 4$, corresponding to the late stage of wave breaking, the number of droplets decreases significantly as most of them fall back into the water body.

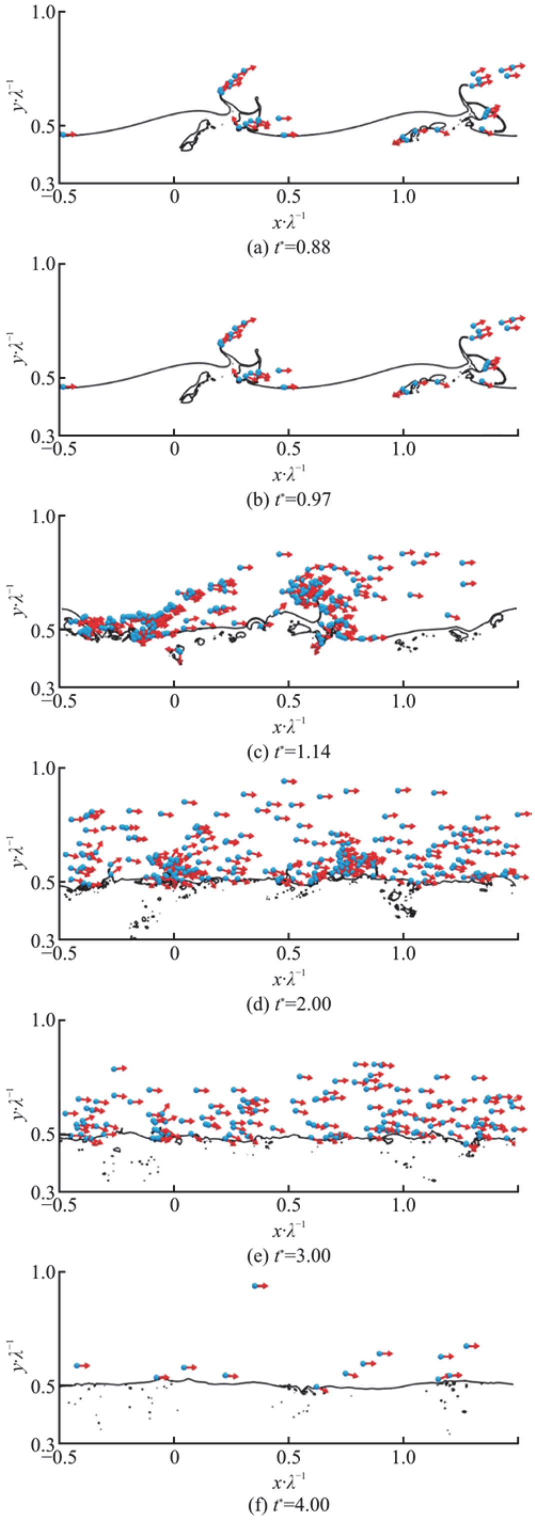

Fig. 9 Instantaneous droplet distribution, where the blue circles represent droplets and the red arrows indicate the direction of the droplets

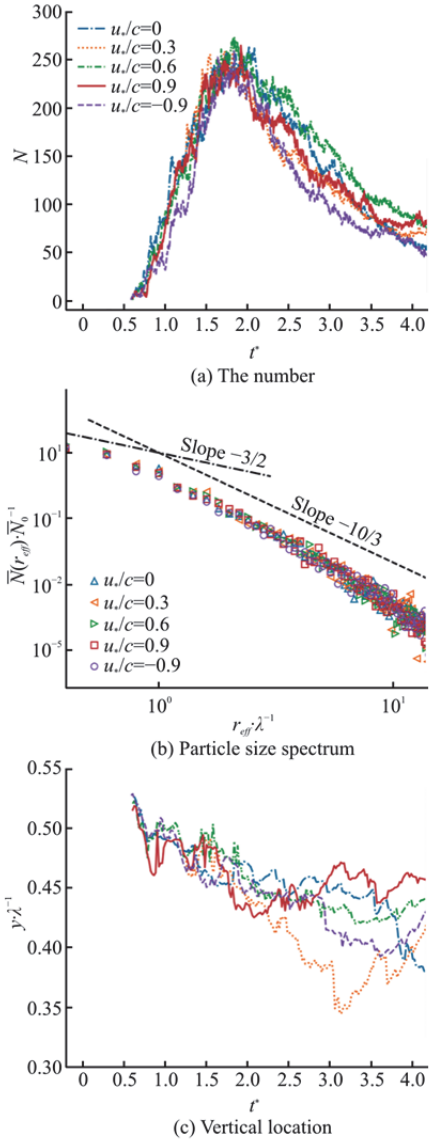

Fig. 10 Bubble distribution characteristics

Figure 10 illustrates the characteristics of bubble distribution during the wave breaking process. Figure 10(a) shows the temporal evolution of the total bubble count. Overall, the number of bubbles exhibits an initial increase followed by a gradual decrease. Notably, no significant increase in bubble quantity is observed under wind forcing conditions. Figure 10(b) presents the bubble size distribution spectra. Across all five cases, a high degree of consistency is observed, and the bubble size distribution follows a power-law scaling of –10/3. Figure 10(c) displays the vertical distribution of the bubble cloud centroids. After $t^* = 2$, significant differences emerge among the cases. As u_* / c increases, the vertical position of the centroid rises. This trend is attributed to intensified surface breakup under higher wind speeds, which drives the bubble cloud closer to the free surface, resulting in shallower vertical distribution.

4. Conclusions

In this study, numerical simulations are conducted to investigate the breaking of steep waves under wind forcing conditions for cases with $u_* / c = 0, 0.3, 0.6, 0.9, -0.9$. Unlike many previous studies[16-20] that primarily focused on wind-driven wave growth, the present work emphasizes the influence of wind forcing on the wave breaking process. Key aspects analyzed include energy evolution[21], droplet generation[22], and bubble dynamics[23]. The main conclusions are summarized as follows:

(1) Wave breaking is found to transfer part of the water's energy into the air, leading to accelerated energy dissipation in the air phase. Under strong wind conditions, the wind significantly enhances wave motion, resulting in a marked increase in turbulent kinetic energy and dissipation rate in the water.

(2) Wind forcing promotes higher droplet splashing, consistent with observed marine spray phenomena. These droplets primarily originate from the jet tip influenced by wind, and their subsequent trajectories are governed by both initial splash speed and local turbulent fluctuations. This causes the droplets to float in the air, greatly extending their existence time.

(3) The bubble size distribution generated by wave breaking follows a –10/3 power law across all cases. While the total bubble count remains largely unaffected by wind, higher wind speeds cause the vertical centroid of the bubble cloud to shift toward shallower depths due to intensified surface breaking.

This study provides useful insights into wave breaking, marine spray, and foam flow dynamics. Future work will be extended to fully three-dimensional simulations to further explore the impact of turbulent wind structures, particularly vortical features, on wave breaking behavior[24-26].

Conflict of interest

All authors declare that there are no other competing interests.

References

[1] Deane G B, Stokes M D. Scale dependence of bubble creation mechanisms in breaking waves [J]. *Nature*, 2002, 418(6900): 839-844.

[2] Deike L. Mass transfer at the ocean-atmosphere interface: The role of wave breaking, droplets, and bubbles [J]. *Annual Review of Fluid Mechanics*, 2022, 54(1): 191-224.

[3] McAllister M L, Draycott S, Calvert R, et al. Three-dimensional wave breaking [J]. *Nature*, 2024, 633(8030): 601-607.

[4] Wang Z, Yang J, Stern F. High-fidelity simulations of bubble, droplet and spray formation in breaking waves [J]. *Journal of Fluid Mechanics*, 2016, 792: 307-327.

[5] Deike L, Popinet S, Melville W K. Capillary effects on

wave breaking [J]. *Journal of Fluid Mechanics*, 2015, 769: 541-569.
[6] Hu Y, Liu C, Yang X, et al. Numerical investigation of the plunging breaker under various wave slopes: Characteristics of spray droplets and air entrainment [J]. *Ocean Engineering*, 2024, 303: 117635.
[7] Hu Y, Liu C, Yang X, et al. Numerical study of bubble rise in plunging breaking waves [J]. *Physics of Fluids*, 2024, 36(5): 057126.
[8] Li T, Shen L. The principal stage in wind-wave generation [J]. *Journal of Fluid Mechanics*, 2022, 934: A41.
[9] Yousefi K, Veron F, Buckley M P. Momentum flux measurements in the airflow over wind-generated surface waves [J]. *Journal of Fluid Mechanics*, 2020, 895: A15.
[10] Phillips O M. On the generation of waves by turbulent wind [J]. *Journal of Fluid Mechanics*, 1957, 2(5): 417-445.
[11] Miles J W. On the generation of surface waves by shear flows [J]. *Journal of Fluid Mechanics*, 1957, 3(2): 185-204.
[12] Yang Z, Deng B Q, Shen L. Direct numerical simulation of wind turbulence over breaking waves [J]. *Journal of Fluid Mechanics*, 2018, 850: 120-155.
[13] Chai B, Liu C, Hu Y, et al. Critical condition for wind-driven wave breaking with the effect of surface tension [J]. *Ocean Engineering*, 2024, 311: 118913.
[14] Popinet S. Gerris: A tree-based adaptive solver for the incompressible Euler equations in complex geometries [J]. *Journal of Computational Physics*, 2003, 190(2): 572-600.
[15] Popinet S. An accurate adaptive solver for surface-tension-driven interfacial flows [J]. *Journal of Computational Physics*, 2009, 228(16): 5838-5866.
[16] Wu J, Popinet S, Deike L. Revisiting wind wave growth with fully coupled direct numerical simulations [J]. *Journal of Fluid Mechanics*, 2022, 951: A18.
[17] Scapin N, Wu J, Farrar J T, et al. Momentum fluxes in wind-forced breaking waves [J]. *Journal of Fluid Mechanics*, 2025, 1009: A20.
[18] Feddersen F, Hanson K, Mostert W, et al. Modelling wind-induced changes to overturning wave shape [J]. *Journal of Fluid Mechanics*, 2024, 1000: A48.
[19] Wu J, Deike L. Wind wave growth in the viscous regime [J]. *Physical Review Fluids*, 2021, 6(9): 094801.
[20] Chen H, Zou Q. Geometry of deep and intermediate water breaking waves influenced by wind speed and direction [J]. *Physics of Fluids*, 2022, 34(8): 087126.
[21] Liu S, Wang H, Bayeul-Lainé A C, et al. Wave statistics and energy dissipation of shallow-water breaking waves in a tank with a level bottom [J]. *Journal of Fluid Mechanics*, 2023, 975: A25.
[22] Erinin M A, Liu C, Wang S D, et al. Plunging breakers. Part 2. Droplet generation [J]. *Journal of Fluid Mechanics*, 2023, 967: A36.
[23] Li R, Yang Z, Zhang W. Numerical investigation of mixed-phase turbulence induced by a plunging jet [J]. *Journal of Fluid Mechanics*, 2024, 979: A27.
[24] Shao Y, Song B, Wan D, et al. Numerical study of air entrainment mechanisms and vortical structures in breaking waves [J]. *Ocean Engineering*, 2025, 341: 122569.
[25] Li Z, Zhang X, Wan D. Research progress on the hydrodynamic performance of water-air-bubble mixed flows around a ship [J]. *Journal of Hydrodynamics*, 2022, 34(2): 171-188.
[26] Shao Y, Wang W, Zhang G, et al. Numerical simulations of breaking waves generated by a 3-D submerged hydrofoil [J]. *Journal of Hydrodynamics*, 2025, 37(1): 35-49.